Am J Physiol Lung Cell Mol Physiol 318: L65–L75, 2020.
First published October 9, 2019; doi:10.1152/ajplung.00103.2019.

RESEARCH ARTICLE | *Translational Physiology*

Synchrotron-based phase-contrast micro-CT as a tool for understanding pulmonary vascular pathobiology and the 3-D microanatomy of alveolar capillary dysplasia

Christian Norvik,[1]* Christian Karl Westöö,[1]* Niccolò Peruzzi,[2] Goran Lovric,[3,4] Oscar van der Have,[1] Rajmund Mokso,[5] Ida Jeremiasen,[1] Hans Brunnström,[6] Csaba Galambos,[7] Martin Bech,[2] and Karin Tran-Lundmark[1]

[1]*Department of Experimental Medical Science, Lund University, Lund, Sweden;* [2]*Medical Radiation Physics, Department of Clinical Sciences, Lund University, Lund, Sweden;* [3]*Centre d'Imagerie BioMédicale, École Polytechnique Fédérale de Lausanne, Lausanne, Switzerland;* [4]*Swiss Light Source, Paul Scherrer Institute, Villigen, Switzerland;* [5]*Max IV Laboratory, Lund University, Lund, Sweden;* [6]*Division of Oncology and Pathology, Department of Clinical Sciences, Lund University, Lund, Sweden; and* [7]*Children's Hospital Colorado, Department of Pathology and Laboratory Medicine, Aurora, Colorado*

Submitted 4 March 2019; accepted in final form 26 September 2019

Norvik C, Westöö CK, Peruzzi N, Lovric G, van der Have O, Mokso R, Jeremiasen I, Brunnström H, Galambos C, Bech M, Tran-Lundmark K. Synchrotron-based phase-contrast micro-CT as a tool for understanding pulmonary vascular pathobiology and the 3-D microanatomy of alveolar capillary dysplasia. *Am J Physiol Lung Cell Mol Physiol* 318: L65–L75, 2020. First published October 9, 2019; doi:10.1152/ajplung.00103.2019.—This study aimed to explore the value of synchrotron-based phase-contrast microcomputed tomography (micro-CT) in pulmonary vascular pathobiology. The microanatomy of the lung is complex with intricate branching patterns. Tissue sections are therefore difficult to interpret. Recruited intrapulmonary bronchopulmonary anastomoses (IBAs) have been described in several forms of pulmonary hypertension, including alveolar capillary dysplasia with misaligned pulmonary veins (ACD/MPV). Here, we examine paraffin-embedded tissue using this nondestructive method for high-resolution three-dimensional imaging. Blocks of healthy and ACD/MPV lung tissue were used. Pulmonary and bronchial arteries in the ACD/MPV block had been preinjected with dye. One section per block was stained, and areas of interest were marked to allow precise beam-alignment during image acquisition at the X02DA TOMCAT beamline (Swiss Light Source). A ×4 magnifying objective coupled to a 20-μm thick scintillating material and a sCMOS detector yielded the best trade-off between spatial resolution and field-of-view. A phase retrieval algorithm was applied and virtual tomographic slices and video clips of the imaged volumes were produced. Dye injections generated a distinct attenuation difference between vessels and surrounding tissue, facilitating segmentation and three-dimensional rendering. Histology and immunohistochemistry post-imaging offered complementary information. IBAs were confirmed in ACD/MPV, and the MPVs were positioned like bronchial veins/venules. We demonstrate the advantages of using synchrotron-based phase-contrast micro-CT for three-dimensional characterization of pulmonary microvascular anatomy in paraffin-embedded tissue. Vascular dye injections add additional value. We confirm intrapulmonary shunting in ACD/MPV and provide support for the hypothesis that MPVs are dilated bronchial veins/venules.

alveolar capillary dysplasia; imaging; lung; pulmonary hypertension; synchrotron; tomography

INTRODUCTION

Pulmonary vascular anatomy is complex, and pathophysiological conditions presenting as pulmonary hypertension (PH) are associated with remodeling of the pulmonary microvasculature. Untreated PH results in right heart failure and death, and available treatments are far from curative (17). New methods to visualize the complex three-dimensional (3-D) microvascular anomalies of PH are needed for understanding the underlying disease process and for evaluation of novel therapeutic interventions. Synchrotron-based imaging methods are increasingly being used for nondestructive high-resolution 3-D imaging of biological material. However, in the field of medicine the advantages of synchrotron-based imaging have not been fully explored.

In disease states with elevated pulmonary arterial pressure, precapillary anastomotic connections between the pulmonary circulation and the bronchial circulation have been described (14, 20, 32, 39). Such bronchopulmonary anastomoses have been associated with bronchial arterial hypertrophy/dilatation in severe pulmonary arterial hypertension (PAH) (10, 18) and likely cause intrapulmonary right-left shunting in idiopathic PAH (15). As part of the systemic circulation, the majority of bronchial arteries (BA) originate from the proximal descending aorta and supply airways and large pulmonary arteries with oxygenated blood (41). Deoxygenated bronchial blood empties in pulmonary veins mixing with the oxygenated blood returning from the pulmonary circulation. Only a minor percentage is believed to empty into systemic veins (13%) under normal conditions (4). Precapillary bronchopulmonary anastomoses could very well explain the exacerbated arterial hypoxemia seen in some PH patients in response to exercise (29, 40). During extreme exercise or catecholamine stress, recruitment of intrapulmonary shunt vessels has been demonstrated to occur even in healthy subjects, as pulmonary blood flow and regional vascular pressures increase (11, 22). Whether the

* C. Norvik and C. K. Westöö contributed equally to this work.

Address for reprint requests and other correspondence: K. Tran-Lundmark, Dept of Experimental Medical Science, Lund Univ., BMC C12, 221 84 Lund, Sweden (e-mail: Karin.tran_lundmark@med.lu.se).

intrapulmonary shunt vessels described in PH are part of the pathology or serve as alternative decompressing routes limiting the increase in pulmonary arterial pressure, or both, has not been established. To fully understand how intrapulmonary right-left shunting contribute to PH pathology, the 3-D anatomy of intrapulmonary bronchopulmonary anastomoses (IBAs) in different forms of PH needs further assessment.

Alveolar capillary dysplasia with misalignment of pulmonary veins (ACD/MPV) is one of the most severe forms of neonatal PH. Respiratory failure usually occurs within 48 h of life and lung transplantation is the only treatment. The histopathological features include medial hypertrophy of small pulmonary arteries and muscularization of distal arterioles, a decreased number of pulmonary capillaries, thickened interalveolar septa containing dysplastic capillaries, and misaligned pulmonary veins (MPV) positioned adjacent to arteries and bronchioles (2, 9). Exactly how these features explain the disease process of ACD/MPV remains uncertain. However, recent 3-D reconstructions of serial lung tissue sections from two infants with ACD/MPV revealed IBAs connecting pulmonary and bronchial arteries (16). In addition, it has been suggested that MPVs are pathologically dilated bronchial veins, dilated due to increased flow caused by intrapulmonary right-left shunting as a result of the markedly remodeled pulmonary arteries and the dysplastic pulmonary capillary network (7, 14).

To elucidate the 3-D microanatomy of pathological changes using standard histological techniques only has proven challenging. Serial sectioning followed by computer-assisted 3-D reconstruction of microanatomical structures has provided important information on vascular lesions and anastomotic vessels in PH research (14, 42). However, the procedure is laborious, time-consuming, and nonscalable.

Laboratory-based microcomputed tomography (micro-CT) of paraffin-embedded lung tissue generates volumetric data in a nondestructive way, which allows for 3-D reconstruction of features of interest (38). The tissue is untouched and available for subsequent histological and immunohistochemical characterization. However, in conventional laboratory-based mi-

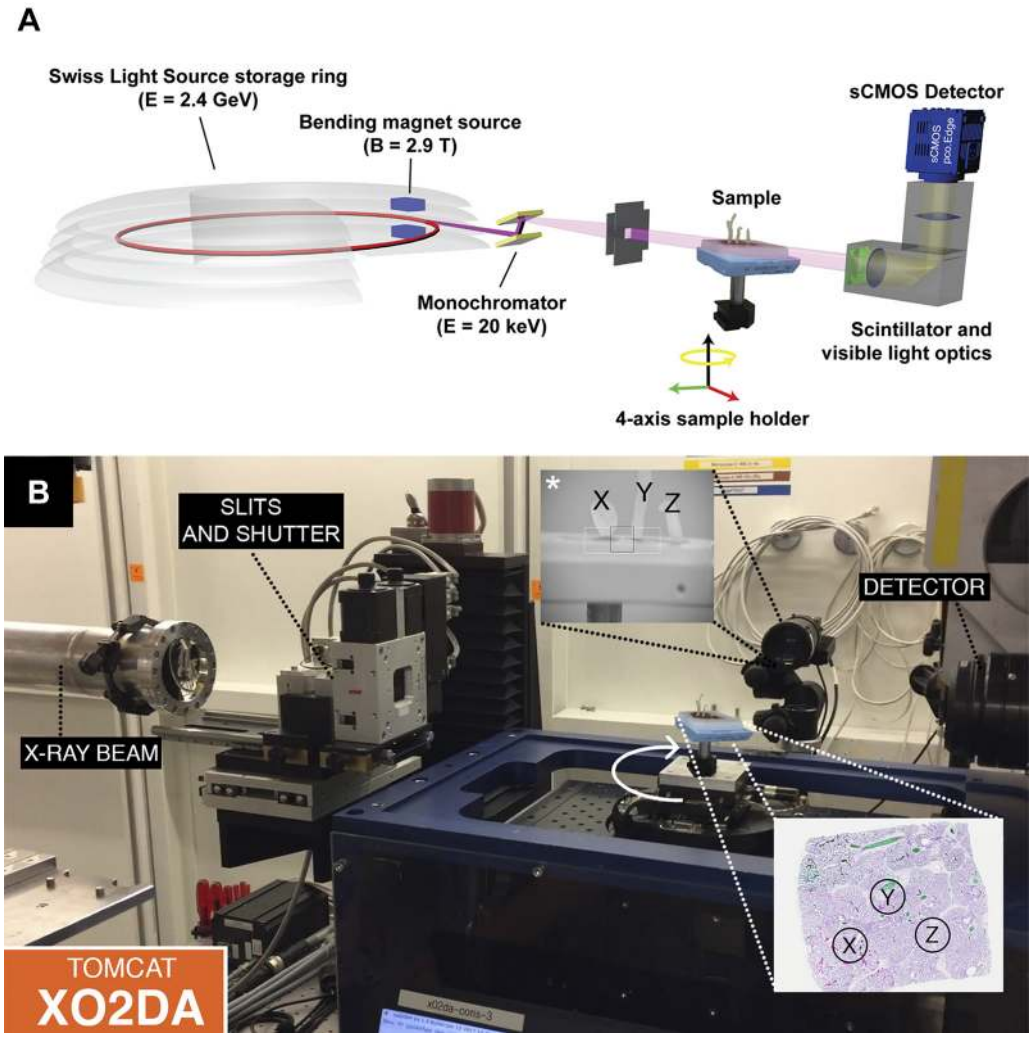

Fig. 1. The TOMCAT beamline at the Swiss Light Source, sample preparation, and experimental set-up. *A*: schematic drawing of the beamline set-up. The X-rays travel from left to right, through the sample, toward the detector. *B*: the positioning of the sample in the experimental hutch at TOMCAT is shown. The paraffin-embedded tissue was placed on the 4-axis sample holder, attached by melted wax. For aligning the sample and to assure that the respective area of interest stays central throughout a 180° rotation, a so-called off-beam sample alignment procedure was used (23). For this reason, wax markers outlining the areas of interest (marked by *X*, *Y*, and *Z*) were placed on top of the sample and aligned with a visible light camera. In *B*, the camera projection (white asterisk) shows the view from the control room, where the crosshairs and the rectangle indicate the center and size of the X-ray beam respectively.

cro-CT setups, contrast is produced by the absorption of X-rays traversing the tissue. Lung tissue (soft tissue) exhibits relatively low and homogenous absorption levels and therefore yields low contrast volumetric data, unless stained with contrast-enhancing agents before image acquisition (8, 31). The low contrast limits the ability to resolve fine detail and makes the acquired image data less comparable to histology and immunohistochemistry. Fortunately, X-rays interacting with matter are not only absorbed but also undergo a phase shift (by refraction). This is utilized in X-ray phase-contrast imaging, which provides enhanced soft tissue contrast and thereby minimizes loss of fine detail (27). Typically, high-quality phase-contrast imaging requires highly coherent X-rays, which are only available at synchrotron sources. Synchrotron-based phase-contrast micro-CT enables unparalleled spatial resolution at the micrometer-scale to be achieved in a small volume of interest in weakly absorbing and/or uniformly dense tissue.

In this study, we explore the value of using synchrotron-based phase-contrast micro-CT for 3-D interpretation of pulmonary vascular pathology by studying the microanatomy of normal lung and the microvascular anomalies of ACD/MPV in archived paraffin-embedded tissue.

METHODS

Tissue selection. One block of formalin-fixed paraffin-embedded tissue from the left lung of a 2-wk-old patient with ACD/MPV was selected for imaging and subsequent complete histological serial sectioning. Tissue samples from the same patient were used in a previous study exploring the pathobiology of ACD/MPV by serial sectioning (16). One block of archived formalin-fixed paraffin-embedded pulmonary tissue from an age-matched neonate, who died from cardiovascular arrest of unknown cause and where no pulmonary pathology had been observed, was selected for imaging to serve as control tissue. All tissues were provided by the Department of Pathology, University of Colorado School of Medicine. The study was approved by the Colorado Multiple Institutional Review Board. Samples were deidentified and the use of archived tissue for imaging and histology was approved by the regional ethical review board in Lund, Sweden (Dnr 2017/597).

Tissue preparation: dye injections. In the ACD/MPV lung, pulmonary and bronchial arteries had been injected with dyes during the autopsy. The heart-lung block was removed according to routine autopsy protocol. The bronchial arteries (BA) were isolated after clamping of the ductus arteriosus, aortic arch, and distal thoracic aorta. The isolated aortic segment containing the BA branches was injected with blue dye. Subsequently, the left pulmonary artery was injected with green dye. The dyes (CDI's Tissue Marking Dye;

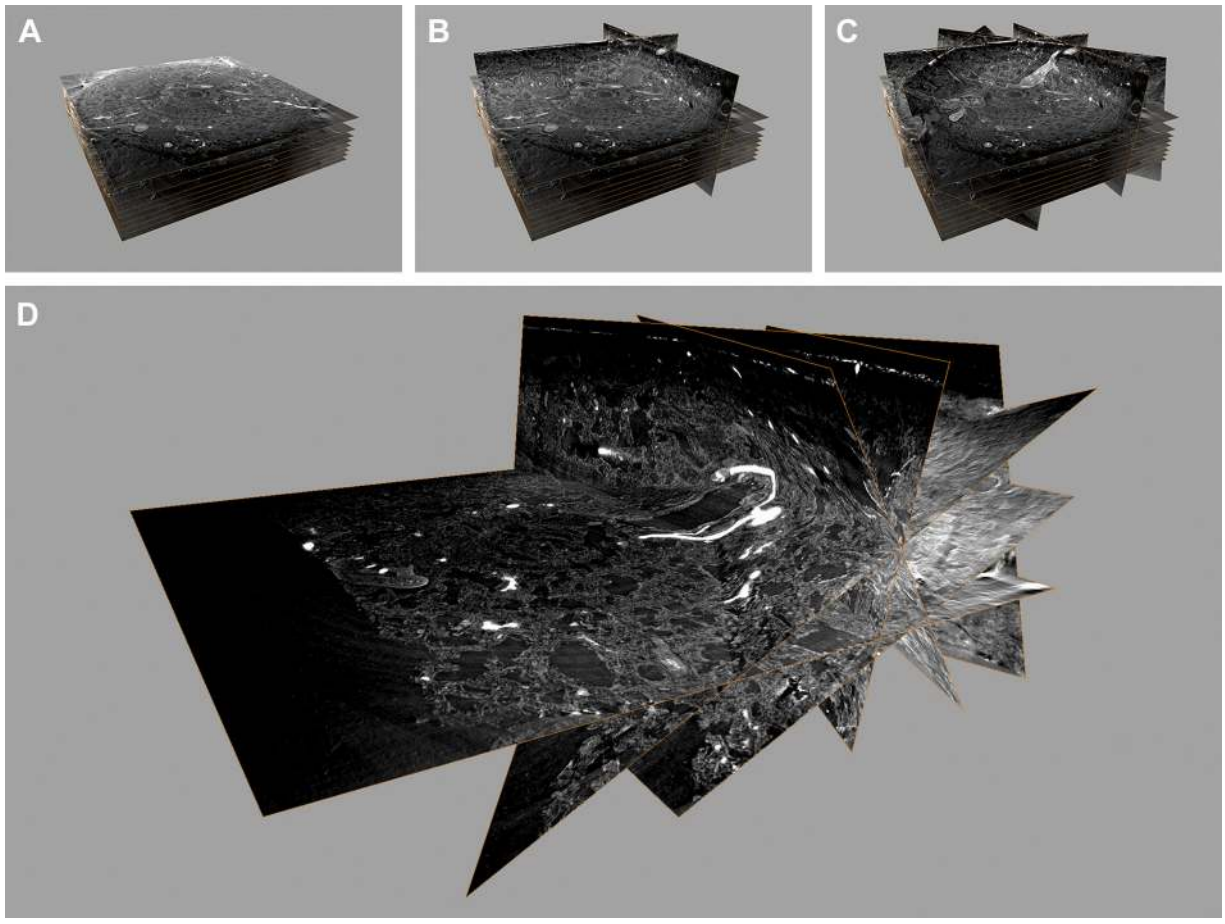

Fig. 2. Image processing. *A*: following image acquisition at the TOMCAT beamline, and subsequent phase retrieval and tomographic reconstruction, the resulting volumetric data sets, each representing 1 scanned volume of interest ($4.2 \times 4.2 \times 3.5$ mm^3), were saved as stacks of TIFF files. Each stack was composed of 2,160 image sections at 16-bit pixel depth. These could be opened and viewed individually or as a stack. *B–D*: the stacks could also be resliced to create new (virtual) image sections from different angles using Amira. Different virtual sections could subsequently be combined to visualize the position and complete course of vessels and vascular connections in the volumetric data. *D* illustrates how Fig. 5*D* was generated.

Cancer Diagnostics, Durham, NC) were diluted with an equal volume of tap water to ensure low viscosity. Twenty-mL syringes equipped with 22-gauge needles were used for the injections. After needle insertion, clamps were used to secure its position in the vessel before initiation of injections. The injections were performed with manually applied semi-gentle pressure and lasted approximately 5 min. During BA injections, minor leakage through unclamped intercostal arteries was observed. After completion of the injections, no dye was present in the heart, eliminating the possibility of extrapulmonary right-left shunting of dye. The lungs were subsequently inflated with formalin and embedded in paraffin.

The control lung tissue had not been injected with any dyes before routine fixation and embedding procedures and was therefore also used to evaluate the method protocol when applied to archived formalin-fixed paraffin-embedded lung tissue. Imaged control vessels in this study are therefore void of any dye.

Tissue preparation: selection of areas of interest. One section from each sample was prepared and stained with hematoxylin-eosin (H&E) using standard protocols. The stained sections were scanned and digitalized using an Aperio ScanScope digital slide scanner (Leica Microsystems, Wetzlar, Germany). Five areas from each sample containing characteristic vascular pathology/control vessels were selected and marked on the digital images. This was necessary for subsequent beam alignment as described below and in Fig. 1*B*. Areas that contained air pockets were avoided, since air trapped during embedding produces significant artifacts.

Synchrotron-based phase-contrast micro-CT. The imaging was performed at the X02DA TOMCAT beamline of the Swiss Light Source at the Paul Scherrer Institute (Villigen, Switzerland). The X-ray beam, produced by a 2.9 T super-bending magnet acting on a 2.4-GeV storage ring, was monochromatized with a double-multilayer monochromator and tuned to an energy of 21 keV. A ×4 magnifying objective coupled to a 20-μm thick scintillating material and a sCMOS detector were used, resulting in a field-of-view of 4.2 × 3.5 mm^2 and an effective pixel size of 1.63 × 1.63 μm^2. A sample-to-detector distance of 19 cm was set for producing sufficient edge-enhancement originating from the Fresnel interference pattern. For each scanned volume of interest, 1,801 projections were acquired with 80-ms single-projection exposure time, resulting in a total scan time of ~2.4 min. Figure 1*A* shows a schematic drawing of the beamline set-up, and Fig. 1*B* shows the experimental hutch at the X02DA TOMCAT beamline.

The paraffin blocks were attached to sample holders (Fig. 1*B*) using melted beeswax (easy to remove when solidified). The samples were then placed on the rotational axes system, which allows for precise alignment and continuous rotation (upon tomographic acquisition, the samples are rotated 180°). Before this, markers of wax were placed on the blocks over the preselected areas of interest. As shown in Fig. 1*B*, the wax markers were essential for beam alignment. Several areas of interest per sample required markers of different shapes to easily couple each acquired data set to its actual location within the sample.

Image processing. Phase retrieval was performed utilizing the algorithm by Paganin et al. (30). Subsequently, tomographic reconstruction was done using the gridrec algorithm (25). Each scanned volume of interest (4.2 × 4.2 × 3.5 mm^3) was saved as a volumetric data set composed of 2,160 image sections at 16-bit pixel depth. Data visualization and analysis were performed in ImageJ (34) (https://imagej.net/plugins/volume-viewer.html). Amira was used for segmentation and 3-D rendering of vessels and airways, as well as for capturing video clips of the processed volumes. The injected dye worked as a radiodense contrast agent appearing as white in the tomographic data. The intensity value of the pixels representing the injected dye therefore significantly exceeds that of pixels representing vessel walls, airways, alveolar septa, and erythrocytes. This allowed for automatic segmentation and 3-D rendering of dye-filled vessels in the ACD/MPV tissue. Manual segmentation was required for 3-D rendering of

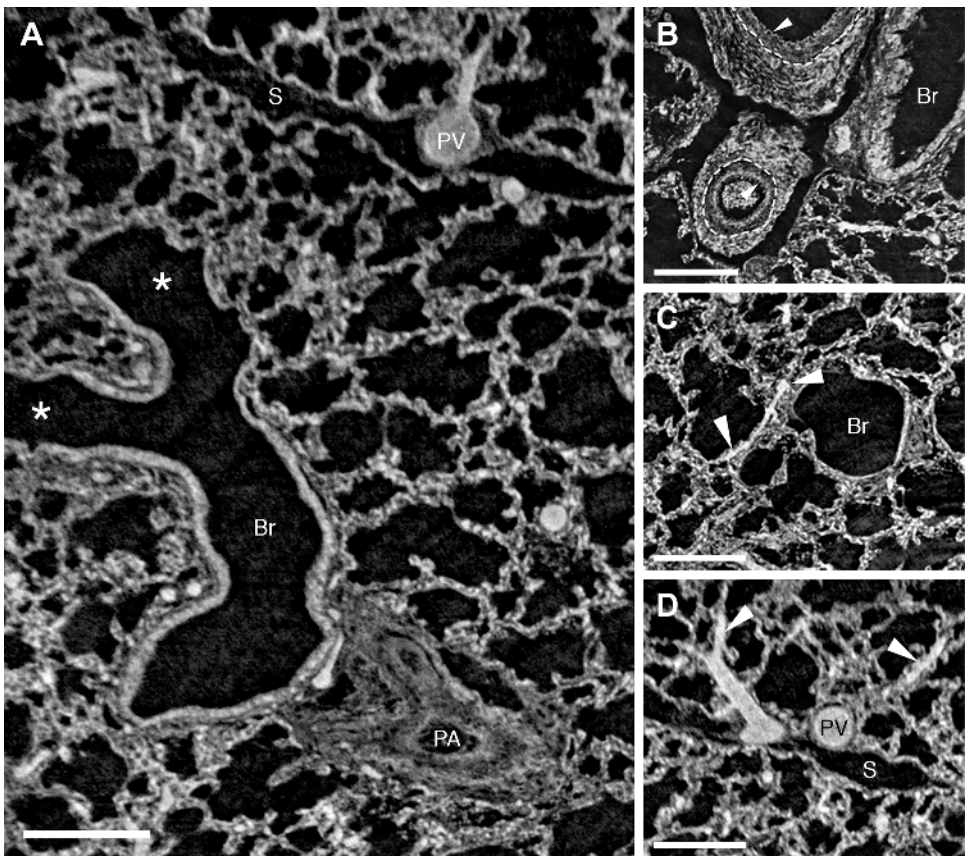

Fig. 3. Microanatomy of the normal neonatal lung. *A*: normal neonatal lung tissue. A bronchiole (Br), accompanied by a pulmonary artery (PA), divides to form respiratory bronchioles/alveolar ducts (white asterisks). Located away from the bronchovascular bundle, a pulmonary vein (PV) containing erythrocytes is positioned in adjacent septa (S). The same area can be seen in Supplemental Video S1 (https://doi.org/10.6084/m9.figshare.9746501). *B*: a pulmonary artery and a segment of its parent artery are shown in cross section. The dashed lines delineate the border between the medial layer and the adventitia of the arterial wall. White arrowheads highlight the internal elastic lamina, the border between intima and media. *C*: respiratory bronchiole/alveolar duct (Br) and its surrounding vessels (white arrowheads). *D*: distal branches of the septal pulmonary vein (PV) from *A* draining parenchymal venules (white arrowheads). All scale bars = 200 μm.

noninjected arteries and veins in the control tissue. Vessels of interest were traced within the tomographic volume and the lumen was manually highlighted every 5th-20th slice. The complete 3-D course of each vessel of interest was then rendered by interpolating the position and size of the lumen in intermediate slices. Manual segmentation was also required for 3-D rendering of airways.

Reslicing the volumetric data and combining virtual sections. Figure 2 shows how Amira was used for reslicing a volume to generate virtual sections from any angle of interest. Virtual sections at different angles were combined to capture the entire course of vessels and/or vascular connections in one single image, without using segmentation and 3-D rendering. This technique does not require vascular contrast injections.

Histology and immunohistochemistry. Following image acquisition, complete serial sectioning of the ACD/MPV sample was performed. Every fifth section was selected for histochemical and immunohistochemical staining. H&E, elastica van Gieson, and Alcian blue/periodic acid-Schiff stainings were performed by the Department of Pathology, Skåne University Hospital (Lund, Sweden), according to standard protocols used for clinical samples. Immunostaining for endothelial cells was done in a Ventana Benchmark Ultra automatic slide stainer (Ventana-Roche Diagnostic, Oro Valley, AZ) using a CD31 anti-human mouse monoclonal primary antibody (clone JC70A, cat. no. M0823; DAKO, Glostrup, Denmark; dilution 1:40, 32-min incubation). Cell Conditioning 1 (CC1; Ventana-Roche) was used for antigen retrieval and OptiView DAB (Ventana-Roche) for detection.

Identification of different vessel types. Because of the relatively small blood volumes that are normally received by the bronchial circulation (only ~1% of the total cardiac output), bronchial vessels are minute and difficult to identify in normal lung sections (41). Physiological intrapulmonary shunting in utero has previously been described, resulting in an increased volume load on the bronchial circulation (26, 33). Therefore, bronchial arteries and veins are distended and thereby easier to identify in neonatal lung tissue, when compared with adult lung tissue.

In the volumetric data, vessels were identified by their size, branching pattern, and positioning relative to airways and interlobular septa. Bronchial vessels were defined by their small size, close relation to airways, and branching pattern, which is not strictly dichotomous. Pulmonary arteries were identified by their relatively larger size, juxtaposed position relative to airways and dichotomous branching pattern. Pulmonary veins were identified by their position in interlobular septa.

Evaluation of histological/immunohistochemical stainings (thickness of the muscular walls and amount of elastin) allowed for further characterization of the different vessel types, i.e., in ACD/MPV, pulmonary arteries are markedly remodeled and thickened, while bronchial arteries are not.

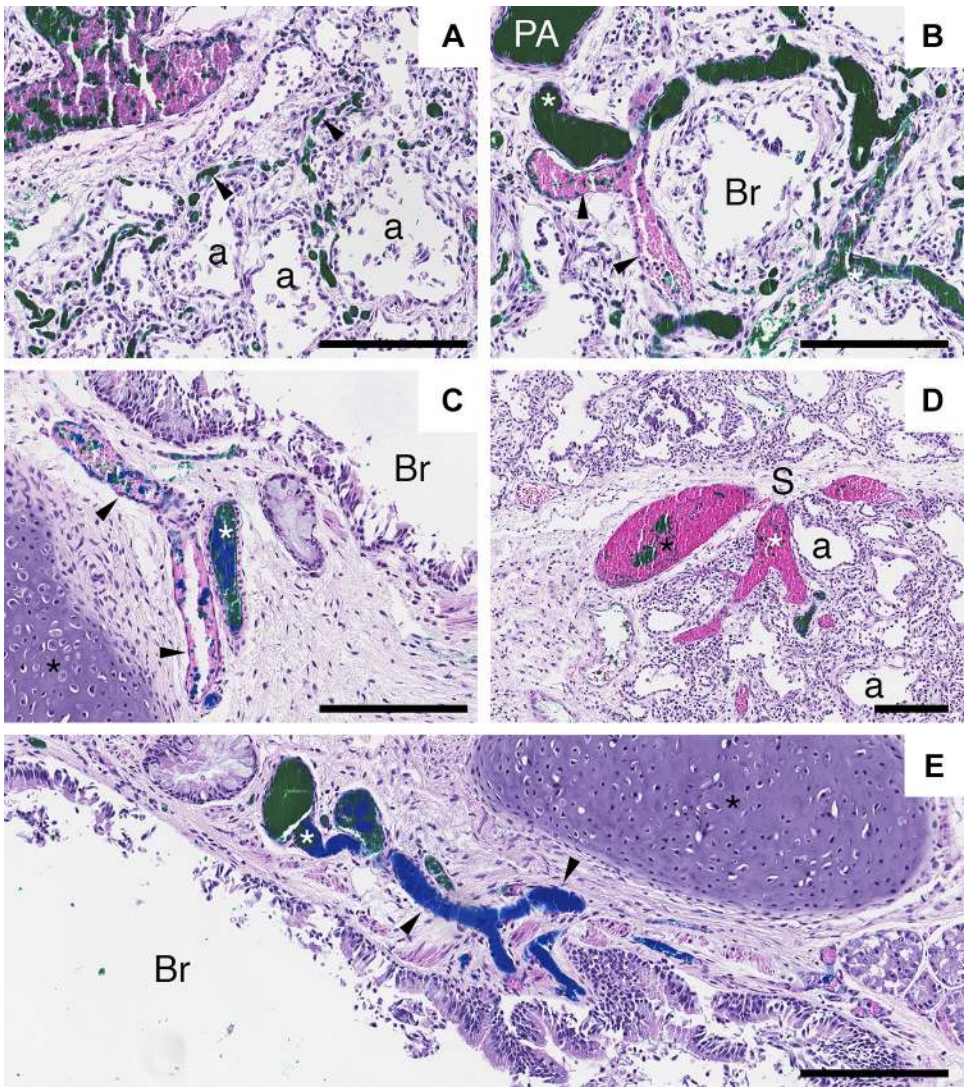

Fig. 4. Histology of alveolar capillary dysplasia with misalignment of pulmonary veins (ACD/MPV) and examination of shunts using dye injections. *A*: thickened interalveolar septa and dye-filled dysplastic capillaries (black arrowheads) with poor connections to the alveolar epithelium lining alveolar spaces (a). *B*: vascular distribution around a small airway (Br). Green dye is present in both a pulmonary artery (PA) as well as in peribronchial microvasculature. From this 2-dimensional image alone, we can only hypothesize the presence of an intrapulmonary bronchopulmonary anastomosis (white asterisk). The black arrowheads highlight an MPV, positioned next to an artery, containing traces of green dye. *C*: a bronchial artery (white asterisk) containing both green and blue dye, next to a large airway (Br) with supporting cartilage (black asterisk). Small amounts of both dyes were also present in an adjacent bronchial vein (black arrowheads). *D*: pulmonary vein (black asterisk) positioned in interlobular septa (S). Green dye could be demonstrated in the septal pulmonary vein, as well as in its venular branches (white asterisk). *E*: branching (bronchial) vessel (black arrowheads) containing only blue dye, next to a large airway (Br) with associated cartilage (black asterisk). In addition, an adjacent vessel containing only green dye, along with one of its branches containing both dyes (white asterisk) is shown. Green dye was localized to the proximal part of the branch, while blue dye is present more distally. All scale bars = 200 μm.

RESULTS

Microanatomy of the normal neonatal lung. The synchrotron-based phase-contrast micro-CT generated highly detailed and informative images of the control lung tissue, as shown in Fig. 3. Individual layers of the walls of pulmonary arteries (≥200 μm in diameter) could be distinguished. As pulmonary arteries were traced to the capillary level, associated airways dividing into respiratory bronchioles/alveolar ducts and connected alveoli were easily identified (Fig. 3*A* and Supplemental Video S1; Supplemental Material is available at https://doi.org/10.6084/m9.figshare.9746501). Video clips provided opportunities to study and trace anatomical structures throughout the tomographic volumes. As demonstrated in Supplemental Video S1, pulmonary veins are separated from the bronchovascular bundle and coalesce in interlobular septa. No apparent misaligned pulmonary veins (MPV) or anastomotic connections between pulmonary arteries and the bronchial circulation were observed in the control lung tissue.

Histology and vascular connections in ACD/MPV. The ACD/MPV lung specimen used for this study had been injected with green and blue dye, in pulmonary arteries and bronchial arteries, respectively. H&E stainings of the sample revealed thickened interalveolar septa and a dysplastic capillary network with poor connection to the alveolar epithelium, consistent with ACD/MPV (Fig. 4). The blue dye was primarily found in proximal bronchial arteries and within MPVs, and the green dye in pulmonary arteries, capillaries, and veins as well as within distal bronchial arteries. Mixing of the dyes, observed in smaller arteries in close proximity of larger airways, within MPVs or bronchial veins, and in dilated bronchial microvessels, indicates that anastomotic connections between the bronchial and pulmonary arterial systems are present (Fig. 4, *C* and *E*). However, as demonstrated in Fig. 4*B*, it is difficult to visualize the anastomoses in detail using only two-dimensional (2-D) data. 3-D vascular rendering is necessary to confirm the presence of such anastomotic connections.

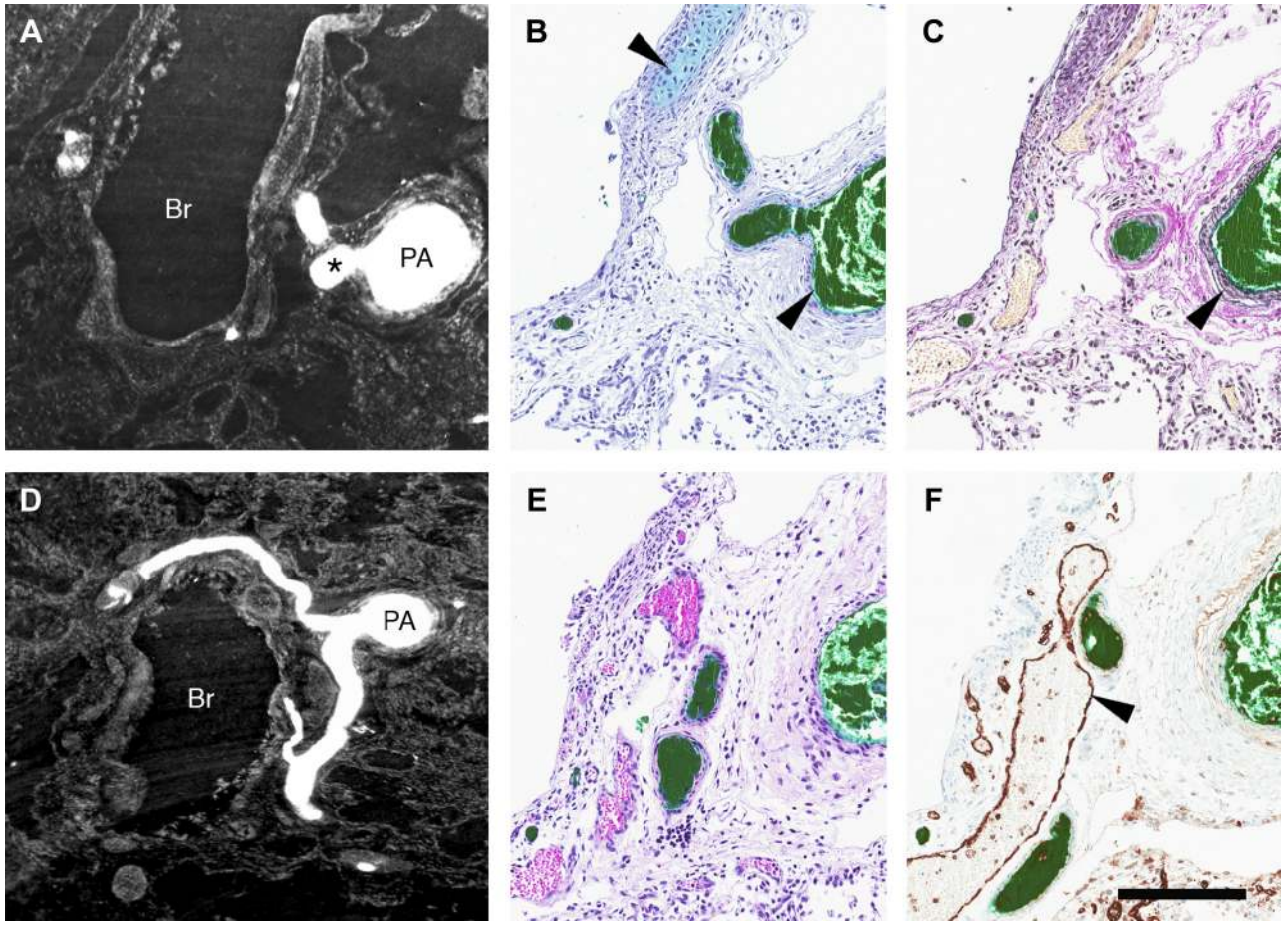

Fig. 5. Combining different virtual sections with histology and immunohistochemistry as a complement to tomography. *A*: possible intrapulmonary bronchopulmonary anastomoses (IBA) (asterisk) in a tomographic image, connecting the pulmonary artery (PA) to bronchial arteries surrounding the airway (Br). A video of the same area/volume shows the entire course of the IBA and confirms the connection (Supplemental Video S2; see (https://doi.org/10.6084/m9.figshare.9746501). *D*: several virtual sections have been combined to visualize the connection in a 2-D image, as described in Fig. 2. Following imaging, the tissue was sectioned and stained. *B*, *C*, *E*, and *F*: different histological stainings of the tissue shown in Supplemental Video S2 (identical plane and orientation). Irradiation had no adverse effects on staining results or on the tissue itself. In *B*, which shows the same level in the tissue as *A*, Alcian blue/periodic acid-Schiff staining shows the presence of proteoglycans in cartilage, as well as in the vascular walls (black arrowheads). Elastica van Gieson, shown in *C*, stains collagen pink and the arrowhead indicates black elastin fibers in the arterial wall. *E* shows a standard hematoxylin-eosin staining and *F* shows immunohistochemistry for endothelial cells using an antibody for CD31 and brown DAB for detection. The arrowhead in *F* marks positive staining in a misaligned pulmonary vein (contained within the bronchovascular bundle, adjacent to an artery) clearly visible in Supplemental Video S2. The scale bar in *F* (200 μm) is valid for *B*, *C*, *E*, and *F*.

Imaging vascular connections and correlating tomography with histology and immunohistochemistry. The presence of IBAs in ACD/MPV was confirmed (Fig. 5 and Supplemental Video S2; see https://doi.org/10.6084/m9.figshare.9746501). The video demonstrates an anastomotic connection between a pulmonary artery and a bronchial artery surrounding a bronchiole. By combining multiple virtual sections at different angles as described in Fig. 2, the vascular anastomosis could be visualized in a 2-D image (Fig. 5*D*).

Histological and immunohistochemical stainings, relevant for studying pulmonary vascular pathology, of serial sections from the imaged ACD/MPV tissue block revealed no adverse effects of the irradiation on morphology (Fig. 4). Stained serial sections corresponding to different levels/virtual sections seen in Supplemental Video S2 were selected and allowed for histological characterization of the IBA and associated vessels (Fig. 5).

When traced in Supplemental Video S2, the continuation of the MPV in Fig. 5*F* and its branches were seen following a tortuous route along the bronchiole, adjacent to bronchial arteries. This confirms previous suggestions of MPVs being pathologically dilated bronchial veins (7, 14).

The advantage of using dye injections, automatic segmentation, and 3-D rendering for understanding vascular connections. The vascular tracer (dye) enabled unhindered 3-D visualization of the vasculature as the surrounding parenchyma could be automatically segmented out and selectively removed.

Automatic segmentation and 3-D rendering of dye-filled vessels within the bronchovascular bundles yielded detailed 3-D reconstructions of IBAs connecting the pulmonary circulation with the bronchial circulation (Fig. 6 and Supplemetnal Videos S3 and S4; see https://doi.org/10.6084/m9.figshare.9746501).

Furthermore, MPVs were observed to be closely associated with peribronchial vasculature, sometimes sharing the adventitial sheaths of bronchial arteries (Fig. 7). Analysis of venous connections in the tomographic data and by histological staining of corresponding sections revealed that MPVs drain peribronchial vasculature to septal pulmonary veins, similar to pulmonary venules that drain dysplastic capillaries. No evidence of downstream obstruction was observed in any of the pulmonary or bronchial veins (Fig. 7).

Manual segmentation and 3-D rendering of noninjected vasculature in the neonatal control lung. Although more laborious when compared with the automatic 3-D reconstruction of dye-filled vessels in the ACD/MPV tissue, manual segmentation and subsequent 3-D rendering of noninjected vasculature in the neonatal control lung yielded precise and comparable 3-D reconstructions. Figure 8 and Supplemental Video S5 (see https://doi.org/10.6084/m9.figshare.9746501) demonstrate that pulmonary venules and veins are separated from the bronchovascular bundle with no dilatation of bronchial veins and no anastomotic connections between pulmonary arteries and the bronchial circulation.

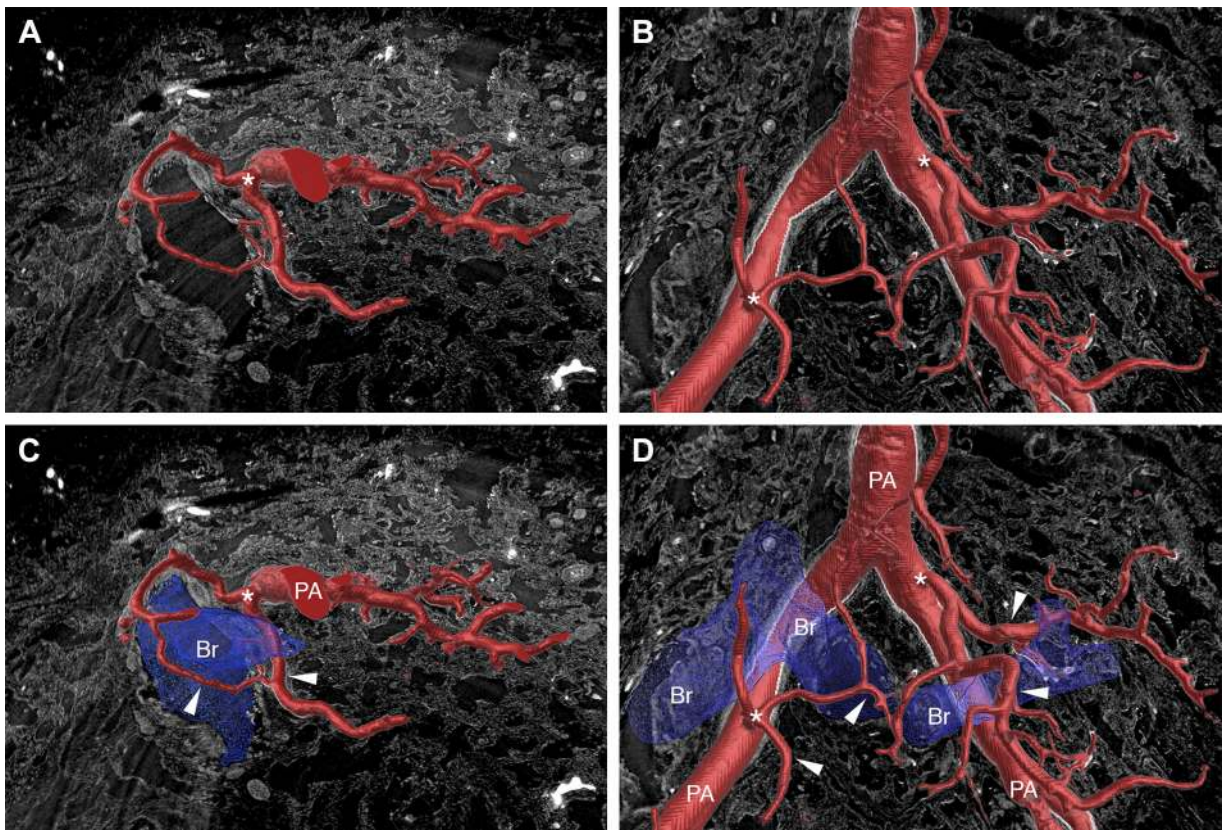

Fig. 6. Segmentation and 3-D rendering to visualize intrapulmonary bronchopulmonary anastomoses (IBAs) and reconstruction of airways. Dye injections allowed for automatic segmentation and 3-D rendering of the vasculature. *A*: same area as in Fig. 5, but with 3-D rendering of the IBA (white asterisk) and its associated dye-filled arteries. *B*: another area with two patent IBAs (white asterisks). *C* and *D*: illustration of how the IBAs (white asterisks) emerge from the parent pulmonary arteries (PA) toward the airways (Br), and connect with bronchial arteries (white arrowheads). Supplemental Videos S3 and S4 (see https://doi.org/10.6084/m9.figshare.9746501) provide a more detailed view of the 3-D rendering in *C* and *D*, respectively.

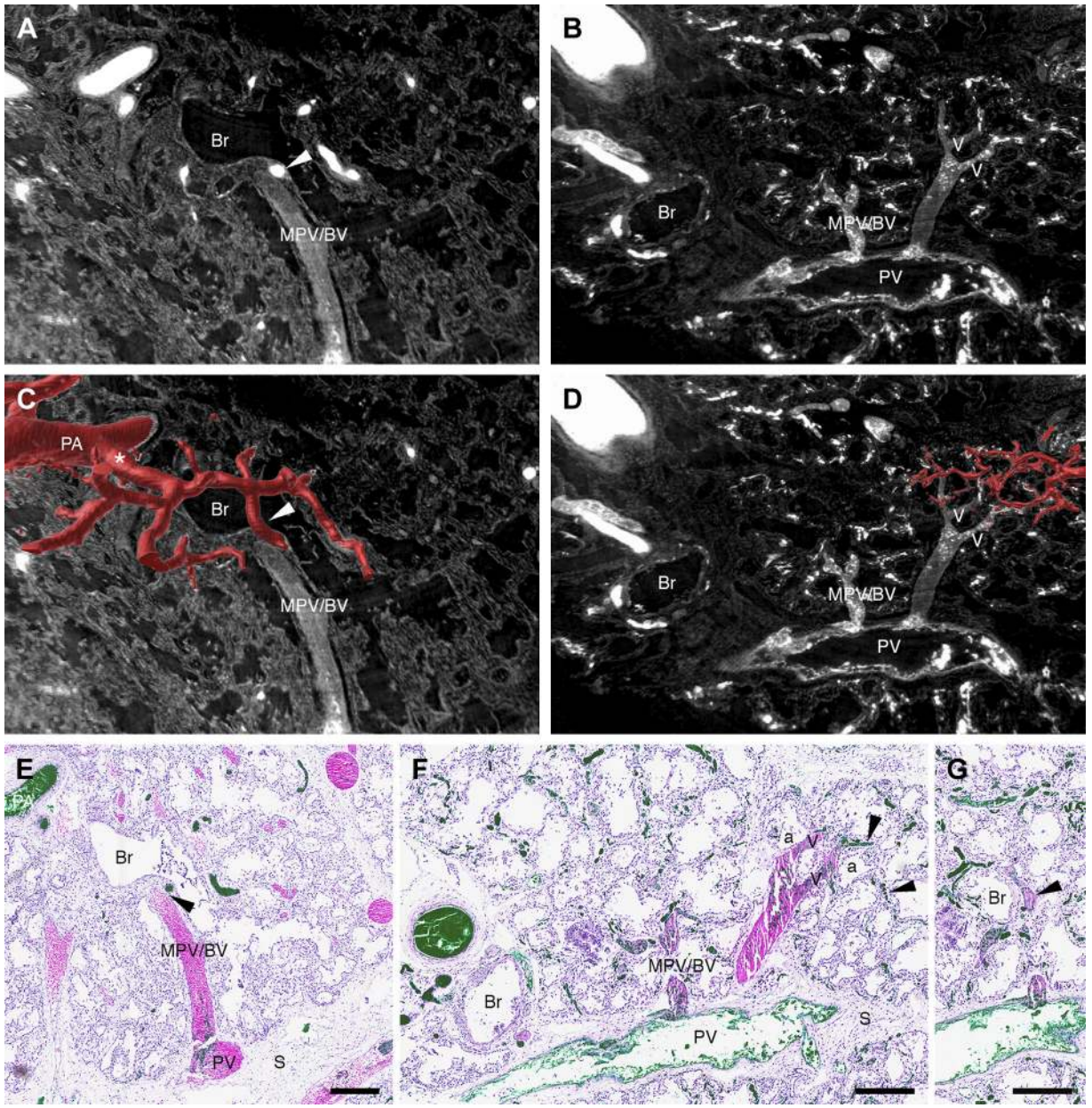

Fig. 7. Venous connections in alveolar capillary dysplasia with misalignment of pulmonary veins (ACD/MPV). *A*: an MPV/dilated bronchial vein (BV) adjacent to a small dye-filled bronchial artery (BA) branch (white arrowhead). *B*: another MPV/BV that empties into a septal pulmonary vein (PV), again without signs of distal obstruction. Converging pulmonary venules (V) draining dysplastic capillaries empties in the same PV. *C*: 3-D rendering of the BA branch (white arrowhead) and its connection to proximal dye-filled arteries above the imaging plane is shown in red. An intrapulmonary bronchopulmonary anastomosis (white asterisk) connects this network of bronchial microvessels surrounding an airway (Br) to an adjacent pulmonary artery (PA). *D*: 3-D rendering of the dye-filled dysplastic capillaries is shown in red. *E*: hematoxylin-eosin (H&E) staining of the same area from *C*, demonstrating how the BA branch and the MPV/BV share the same adventitial sheath (black arrowhead). The MPV/BV empties into a PV in an adjacent interlobular septum (S), with no signs of obstruction. *F*: distribution of the rendered dye-filled dysplastic capillaries (black arrowheads) and associated alveoli (a) in an H&E staining of the same area. "S" marks the interlobular septum in which the PV is positioned. *G*: a proximal section of the MPV/BV (*B*, *D*, and *F*) visualizes its course and position (black arrowhead) adjacent to dye-filled bronchial microvessels surrounding a terminal bronchiole (Br). Scale bars in *E*, *F*, and *G* = 300 μm.

DISCUSSION

High-resolution X-ray imaging of soft tissue is challenging. For paraffin-embedded lung tissue, the poor and homogenous X-ray absorption typically yields low contrast (5). Synchrotron-based phase-contrast micro-CT significantly enhances soft tissue contrast, reducing loss of fine detail, and provides spatial resolutions at the micrometer scale. Submicron resolutions (effective pixel size of 0.16×0.16 μm^2) can be achieved when imaging smaller volumes of interest ($0.4 \times 0.4 \times 0.3$ mm^3). For this study, a $\times 4$ magnifying objective was used to image volumes of interest ($4.2 \times 4.2 \times 3.5$ mm^3) resulting in volumetric data sets with an effective pixel size of 1.63×1.63 μm^2. The larger volume of interest was necessary since the aim of the study

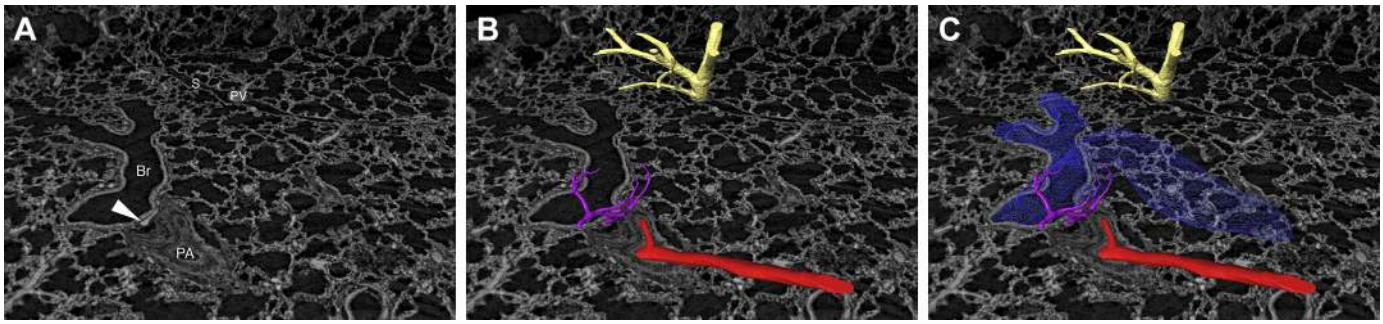

Fig. 8. Manual segmentation and 3-D rendering to visualize noninjected vessels in the neonatal control lung. Here, the area shown in Fig. 3*A* has been captured from a slightly different angle in Amira. *A*: the same structures as shown in Fig. 3*A*: bronchiole (Br), bronchial vessel (arrowhead), pulmonary artery (PA), and pulmonary vein (PV) positioned in septa (S). *B*: manual 3-D reconstructions of PA (red), PV (yellow), and bronchial vessels (purple) are shown. *C*: the additional manual 3-D reconstruction of the bronchiole (blue) elucidates the spatial relationship between each vessel type and said bronchiole. Supplemental Video S5 (https://doi.org/10.6084/m9.figshare.9746501) provides a more detailed view of the manual 3-D reconstructions presented in *C*.

required vessels and their branches/connections to be followed over some distance.

Vascular phase-contrast X-ray imaging has been performed at synchrotron facilities previously. Ex vivo, the cerebrovascular architecture in rats and atherosclerosis in larger vessels in mice have been visualized (3, 43). However, for those studies the tissue had been specially prepared for imaging and the samples were embedded in paraffin post-imaging. This makes histological and immunohistochemical stainings less comparable to the volumetric data, as tissue dimensions are significantly altered during embedding procedures (35). For visualization of airways, synchrotron-based phase-contrast micro-CT has been used to image already paraffin-embedded tissue. The tissue was however treated with contrast-enhancing heavy metal stains before embedding to facilitate identification of structures of interest (1, 19).

Our results show that untreated archived paraffin-embedded lung tissue can be visualized by synchrotron-based phase-contrast micro-CT, with sufficient detail to reveal individual layers in the vascular wall of pulmonary arteries $\geq$200 μm in diameter (Fig. 3*B*). The radiodense green dye injected in the pulmonary vessels in the ACD/MPV tissue facilitated automatic segmentation and 3-D rendering of dye-filled vessels and enabled 3-D characterization of anastomotic connections (Fig. 6). Although no dye was injected in the control tissue, vessels could easily be identified and traced to the capillary level in the volumetric data. Subsequent manual segmentation allowed for precise and comparable 3-D rendering (Fig. 8). Standard pathologic evaluation of serial sections from the imaged tissue revealed no adverse irradiation effects and enabled targeted histological/immunohistochemical assessment of vessels reconstructed in 3-D.

The radiation produced by synchrotron sources enables state of the art X-ray phase-contrast imaging. Its application in pulmonary and vascular research has proven useful for qualitative characterization and quantitative measurements of microanatomical structures of the lung (13, 24). The significantly shorter scan times required for image acquisition with synchrotron-based phase-contrast micro-CT (order of minutes), when compared with conventional laboratory-based micro-CT (order of hours), permit high-resolution in vivo imaging, which has been used to assess vascular responsiveness to drug stimuli and hypoxia in PH animal models (36, 37). Only a limited number of synchrotron facilities are currently available world-wide, and the accessibility of the technique is therefore limited (28). However, in the past years, commissioning of new synchrotron facilities at geographically strategical sites around the world has accelerated and will increase the accessibility to beamlines dedicated for research on biological material (38a). In addition, data acquisition at already operational beamlines is gradually becoming more user friendly. Along with further technical and procedural improvements, an increasing number of researchers will gain access to synchrotron X-ray sources as total experimental times decrease. Ultimately, a transition from synchrotron sources to conventional X-ray sources is crucial for future development of widely available laboratory-based alternatives (12). Advancements are being made and in a recent publication, the potentials of a novel laboratory-based technique for high-resolution phase-contrast tomography were demonstrated by visualization of terminal bronchioles and alveoli in mouse lungs (21).

In this study, synchrotron-based phase-contrast micro-CT and subsequent 3-D analysis in conjunction with standard histological evaluation confirmed the presence of IBAs in ACD/MPV.

In ACD/MPV, the capillary network in the pulmonary circulation is defective, with poor arborization and poor connections between the capillary endothelium and the alveolar epithelium, resulting in a high pulmonary vascular resistance. Based on the results of this study, we argue that right-left shunting occurs via IBAs and that the bronchial circulation is used for shunting blood past the dysplastic capillary bed, which would contribute significantly to the severe hypoxemia associated with the intractable and nonresponsive PH in ACD/MPV patients. Furthermore, MPVs were observed to drain peribronchial vasculature and were found bundled with bronchial arteries, following a route consistent with that of bronchial veins. In line with previous observations, this suggests that MPVs are distended bronchial veins (7, 14). Visualization of venous connections by serial sectioning and histology is challenging. However, the complete course of venules/veins could be traced in the volumetric data, which allowed for assessment of venous connections and downstream obstruction (Fig. 7). As no downstream obstruction was observed, the MPVs/bronchial veins are likely to be dilated by the increased volume load of blood shunted from the pulmonary circulation to the bronchial circulation, via IBAs.

In conclusion, we demonstrate the advantages of utilizing synchrotron-based phase-contrast micro-CT for 3-D character-

ization of pulmonary microvascular anatomy and pathology in archived paraffin-embedded lung samples. This nondestructive method enables 3-D reconstruction and targeted histological/immunohistochemical assessment of features of interest at micrometer-scale resolutions.

ACKNOWLEDGMENTS

We acknowledge the Paul Scherrer Institut, Villigen, Switzerland, for provision of synchrotron radiation beamtime at the TOMCAT beamline X02DA of the Swiss Light Source.

GRANTS

This project was funded by the Swedish Heart-Lung Foundation, the Skåne County Council, Thure Carlsson Memorial Foundation, Svenska Läkaresällskapet, Sten K. Johnson Foundation, and the Crafoord Foundation. We also acknowledge the support of National Organization for Rare Disorders (NORD; Alveolar Capillary Dysplasia with Misalignment of Pulmonary Veins Fund), the Linda Crnic Institute, and the Jayden DeLuca Foundation. Further, this research was supported by the Swedish Research Council grant numbers E0605401 and E0605402.

DISCLOSURES

No conflicts of interest, financial or otherwise, are declared by the authors.

AUTHOR CONTRIBUTIONS

C.N., C.K.W., R.M., and K.T.-L. conceived and designed research; C.N., C.K.W., N.P., G.L., R.M., I.J., H.B., C.G., M.B., and K.T.-L. performed experiments; C.N., C.K.W., N.P., H.B., C.G., and K.T.-L. analyzed data; C.N., C.K.W., H.B., C.G., and K.T.-L. interpreted results of experiments; C.N., C.K.W., G.L., and K.T.-L. prepared figures; C.N., C.K.W., and K.T.-L. drafted manuscript; C.N., C.K.W., N.P., G.L., O.v.d.H., R.M., I.J., H.B., C.G., M.B., and K.T.-L. edited and revised manuscript; C.N., C.K.W., N.P., G.L., O.v.d.H., R.M., I.J., H.B., C.G., M.B., and K.T.-L. approved final version of manuscript.

REFERENCES

1. **Barré SF, Haberthür D, Cremona TP, Stampanoni M, Schittny JC.** The total number of acini remains constant throughout postnatal rat lung development. *Am J Physiol Lung Cell Mol Physiol* 311: L1082–L1089, 2016. doi:10.1152/ajplung.00325.2016.
2. **Bishop NB, Stankiewicz P, Steinhorn RH.** Alveolar capillary dysplasia. *Am J Respir Crit Care Med* 184: 172–179, 2011. doi:10.1164/rccm.201010-1697CI.
3. **Bonanno G, Coppo S, Modregger P, Pellegrin M, Stuber A, Stampanoni M, Mazzolai L, Stuber M, van Heeswijk RB.** Ultra-high-resolution 3D imaging of atherosclerosis in mice with synchrotron differential phase contrast: a proof of concept study. *Sci Rep* 5: 11980, 2015. doi:10.1038/srep11980.
4. **Charan NB, Thompson WH, Carvalho P.** Functional anatomy of bronchial veins. *Pulm Pharmacol Ther* 20: 100–103, 2007. doi:10.1016/j.pupt.2006.03.004.
5. **Clark DP, Badea CT.** Micro-CT of rodents: state-of-the-art and future perspectives. *Phys Med* 30: 619–634, 2014. doi:10.1016/j.ejmp.2014.05.011.
7. **Cullinane C, Cox PN, Silver MM.** Persistent pulmonary hypertension of the newborn due to alveolar capillary dysplasia. *Pediatr Pathol* 12: 499–514, 1992. doi:10.3109/15513819209024200.
8. **de S e Silva JM, Zanette I, Noël PB, Cardoso MB, Kimm MA, Pfeiffer F.** Three-dimensional non-destructive soft-tissue visualization with X-ray staining micro-tomography. *Sci Rep* 5: 14088, 2015. doi:10.1038/srep14088.
9. **Deutsch GH, Young LR, Deterding RR, Fan LL, Dell SD, Bean JA, Brody AS, Nogee LM, Trapnell BC, Langston C, Albright EA, Askin FB, Baker P, Chou PM, Cool CM, Coventry SC, Cutz E, Davis MM, Dishop MK, Galambos C, Patterson K, Travis WD, Wert SE, White FV; Pathology Cooperative Group; ChILD Research Co-operative.** Diffuse lung disease in young children: application of a novel classification scheme. *Am J Respir Crit Care Med* 176: 1120–1128, 2007. doi:10.1164/rccm.200703-393OC.
10. **Dorfmüller P, Günther S, Ghigna MR, Thomas de Montpréville V, Boulate D, Paul JF, Jaïs X, Decante B, Simonneau G, Dartevelle P, Humbert M, Fadel E, Mercier O.** Microvascular disease in chronic thromboembolic pulmonary hypertension: a role for pulmonary veins and systemic vasculature. *Eur Respir J* 44: 1275–1288, 2014. doi:10.1183/09031936.00169113.
11. **Eldridge MW, Dempsey JA, Haverkamp HC, Lovering AT, Hokanson JS.** Exercise-induced intrapulmonary arteriovenous shunting in healthy humans. *J Appl Physiol (1985)* 97: 797–805, 2004. doi:10.1152/japplphysiol.00137.2004.
12. **Endrizzi M.** X-ray phase-contrast imaging. *Nucl Instrum Methods Phys Res A* 878: 88–98, 2018. doi:10.1016/j.nima.2017.07.036.
13. **Fuji S, Matsushita S, Hyodo K, Osaka M, Sakamoto H, Tanioka K, Miyakawa K, Kubota M, Hiramatsu Y, Tokunaga C.** Association between endothelial function and micro-vascular remodeling measured by synchrotron radiation pulmonary micro-angiography in pulmonary arterial hypertension. *Gen Thorac Cardiovasc Surg* 64: 597–603, 2016. doi:10.1007/s11748-016-0684-6.
14. **Galambos C, Sims-Lucas S, Abman SH.** Three-dimensional reconstruction identifies misaligned pulmonary veins as intrapulmonary shunt vessels in alveolar capillary dysplasia. *J Pediatr* 164: 192–195, 2014. doi:10.1016/j.jpeds.2013.08.035.
15. **Galambos C, Sims-Lucas S, Abman SH, Cool CD.** Intrapulmonary bronchopulmonary anastomoses and plexiform lesions in idiopathic pulmonary arterial hypertension. *Am J Respir Crit Care Med* 193: 574–576, 2016. doi:10.1164/rccm.201507-1508LE.
16. **Galambos C, Sims-Lucas S, Ali N, Gien J, Dishop MK, Abman SH.** Intrapulmonary vascular shunt pathways in alveolar capillary dysplasia with misalignment of pulmonary veins. *Thorax* 70: 84–85, 2015. doi:10.1136/thoraxjnl-2014-205851.
17. **Galiè N, Channick RN, Frantz RP, Grünig E, Jing ZC, Moiseeva O, Preston IR, Pulido T, Safdar Z, Tamura Y, McLaughlin VV.** Risk stratification and medical therapy of pulmonary arterial hypertension. *Eur Respir J* 53: 1801889, 2019. doi:10.1183/13993003.01889-2018.
18. **Ghigna MR, Guignabert C, Montani D, Girerd B, Jaïs X, Savale L, Hervé P, Thomas de Montpréville V, Mercier O, Sitbon O, Soubrier F, Fadel E, Simonneau G, Humbert M, Dorfmüller P.** BMPR2 mutation status influences bronchial vascular changes in pulmonary arterial hypertension. *Eur Respir J* 48: 1668–1681, 2016. doi:10.1183/13993003.00464-2016.
19. **Haberthür D, Barré SF, Tschanz SA, Yao E, Stampanoni M, Schittny JC.** Visualization and stereological characterization of individual rat lung acini by high-resolution X-ray tomographic microscopy. *J Appl Physiol (1985)* 115: 1379–1387, 2013. doi:10.1152/japplphysiol.00642.2013.
20. **Humbert M, Guignabert C, Bonnet S, Dorfmüller P, Klinger JR, Nicolls MR, Olschewski AJ, Pullamsetti SS, Schermuly RT, Stenmark KR, Rabinovitch M.** Pathology and pathobiology of pulmonary hypertension: state of the art and research perspectives. *Eur Respir J* 53: 1801887, 2019. doi:10.1183/13993003.01887-2018.
21. **Krenkel M, Töpperwien M, Dullin C, Alves F, Salditt T.** Propagation-based phase-contrast tomography for high-resolution lung imaging with laboratory sources. *AIP Adv* 6: 035007, 2016. doi:10.1063/1.4943898.
22. **Laurie SS, Elliott JE, Goodman RD, Lovering AT.** Catecholamine-induced opening of intrapulmonary arteriovenous anastomoses in healthy humans at rest. *J Appl Physiol (1985)* 113: 1213–1222, 2012. doi:10.1152/japplphysiol.00565.2012.
23. **Lovric G, Mokso R, Schlepütz CM, Stampanoni M.** A multi-purpose imaging endstation for high-resolution micrometer-scaled sub-second tomography. *Phys Med* 32: 1771–1778, 2016. doi:10.1016/j.ejmp.2016.08.012.
24. **Lovric G, Vogiatzis Oikonomidis I, Mokso R, Stampanoni M, Roth-Kleiner M, Schittny JC.** Automated computer-assisted quantitative analysis of intact murine lungs at the alveolar scale. *PLoS One* 12: e0183979, 2017. doi:10.1371/journal.pone.0183979.
25. **Marone F, Stampanoni M.** Regridding reconstruction algorithm for real-time tomographic imaging. *J Synchrotron Radiat* 19: 1029–1037, 2012. doi:10.1107/S0909049512032864.
26. **McMullan DM, Hanley FL, Cohen GA, Portman MA, Riemer RK.** Pulmonary arteriovenous shunting in the normal fetal lung. *J Am Coll Cardiol* 44: 1497–1500, 2004. doi:10.1016/j.jacc.2004.06.064.
27. **Momose A, Takeda T, Itai Y, Hirano K.** Phase-contrast X-ray computed tomography for observing biological soft tissues. *Nat Med* 2: 473–475, 1996. doi:10.1038/nm0496-473.
28. **Mühlfeld C, Wrede C, Knudsen L, Buchacker T, Ochs M, Grothausmann R.** Recent developments in 3-D reconstruction and stereology to

study the pulmonary vasculature. *Am J Physiol Lung Cell Mol Physiol* 315: L173–L183, 2018. doi:10.1152/ajplung.00541.2017.

29. **Paciocco G, Martinez FJ, Bossone E, Pielsticker E, Gillespie B, Rubenfire M.** Oxygen desaturation on the six-minute walk test and mortality in untreated primary pulmonary hypertension. *Eur Respir J* 17: 647–652, 2001. doi:10.1183/09031936.01.17406470.
30. **Paganin D, Mayo SC, Gureyev TE, Miller PR, Wilkins SW.** Simultaneous phase and amplitude extraction from a single defocused image of a homogeneous object. *J Microsc* 206: 33–40, 2002. doi:10.1046/j.1365-2818.2002.01010.x.
31. **Patzelt M, Mrzilkova J, Dudak J, Krejci F, Zemlicka J, Karch J, Musil V, Rosina J, Sykora V, Horehledova B, Zach P.** Ethanol fixation method for heart and lung imaging in micro-CT. *Jpn J Radiol* 37: 500–510, 2019. doi:10.1007/s11604-019-00830-6.
32. **Pump KK.** The bronchial arteries and their anastomoses in the human lung. *Dis Chest* 43: 245–255, 1963. doi:10.1378/chest.43.3.245.
33. **Robertson B.** Postnatal formation and obliteration of arterial anastomoses in the human lung. A microangiographic and histologic study. *Pediatrics* 43: 971–979, 1969.
34. **Schindelin J, Arganda-Carreras I, Frise E, Kaynig V, Longair M, Pietzsch T, Preibisch S, Rueden C, Saalfeld S, Schmid B, Tinevez JY, White DJ, Hartenstein V, Eliceiri K, Tomancak P, Cardona A.** Fiji: an open-source platform for biological-image analysis. *Nat Methods* 9: 676–682, 2012. doi:10.1038/nmeth.2019.
35. **Schneider JP, Ochs M.** Alterations of mouse lung tissue dimensions during processing for morphometry: a comparison of methods. *Am J Physiol Lung Cell Mol Physiol* 306: L341–L350, 2014. doi:10.1152/ajplung.00329.2013.
36. **Schwenke DO, Gray EA, Pearson JT, Sonobe T, Ishibashi-Ueda H, Campillo I, Kangawa K, Umetani K, Shirai M.** Exogenous ghrelin improves blood flow distribution in pulmonary hypertension-assessed using synchrotron radiation microangiography. *Pflugers Arch* 462: 397–406, 2011. doi:10.1007/s00424-011-0992-8.
37. **Schwenke DO, Pearson JT, Kangawa K, Umetani K, Shirai M.** Changes in macrovessel pulmonary blood flow distribution following chronic hypoxia: assessed using synchrotron radiation microangiography. *J Appl Physiol (1985)* 104: 88–96, 2008. doi:10.1152/japplphysiol.00610.2007.
38. **Scott AE, Vasilescu DM, Seal KA, Keyes SD, Mavrogordato MN, Hogg JC, Sinclair I, Warner JA, Hackett TL, Lackie PM.** Three dimensional imaging of paraffin embedded human lung tissue samples by micro-computed tomography. *PLoS One* 10: e0126230, 2015. doi:10.1371/journal.pone.0126230.

38a. Synchrotron sources accelerate. https://www.nature.com/articles/nphoton.2015.76 *Nature Photon* 9: 281, 2015.

39. **Turner-Warwick M.** Precapillary systemic-pulmonary anastomoses. *Thorax* 18: 225–237, 1963. doi:10.1136/thx.18.3.225.
40. **Vodoz JF, Cottin V, Glérant JC, Derumeaux G, Khouatra C, Blanchet AS, Mastroïanni B, Bayle JY, Mornex JF, Cordier JF.** Right-to-left shunt with hypoxemia in pulmonary hypertension. *BMC Cardiovasc Disord* 9: 15, 2009. doi:10.1186/1471-2261-9-15.
41. **Walker CM, Rosado-de-Christenson ML, Martínez-Jiménez S, Kunin JR, Wible BC.** Bronchial arteries: anatomy, function, hypertrophy, and anomalies. *Radiographics* 35: 32–49, 2015. doi:10.1148/rg.351140089.
42. **Yaginuma G, Mohri H, Takahashi T.** Distribution of arterial lesions and collateral pathways in the pulmonary hypertension of congenital heart disease: a computer aided reconstruction study. *Thorax* 45: 586–590, 1990. doi:10.1136/thx.45.8.586.
43. **Zhang MQ, Zhou L, Deng QF, Xie YY, Xiao TQ, Cao YZ, Zhang JW, Chen XM, Yin XZ, Xiao B.** Ultra-high-resolution 3D digitalized imaging of the cerebral angioarchitecture in rats using synchrotron radiation. *Sci Rep* 5: 14982, 2015. doi:10.1038/srep14982.